Chapter VI

Effect of low energy Xe^+ ion irradiation on WS_2 nanosheets

Over the years, ion beam technology has been successfully implemented to modify the properties of various materials [1]. This technique has been used for synthesis and fabrication of nanostructures in a dielectric matrix [1]. The ion implantation in different semiconductors has opened up new means for device applications, such as, nanophotonics, photovoltaics and quantum electronics [2]. Ion beam irradiation offers a suitable strategy to explore the damage effects of nuclear materials in extremely harsh radiation environment [2]. Most recently, the ion beam modification in 2D materials has become a powerful tool to tailor and engineer the properties of various 2D materials. In the past few years, lot many works have been performed on the modification of 2D materials considering ion beam irradiation effect [3]. However, only a little information exists as regards irradiation induced effects on such systems, especially at low energy with nuclear energy loss (S_n) dominant over electronic energy loss (S_e). Wang *et. al.* have irradiated WS_2 nanosheets with 100 keV electron beam and have invariably observed the formation of holes and shrinking of lattice due to gradual decrease of S atoms. [4]. Similarly, the disruption of WS_2 nanotubes from the outer layer to the inside one has been witnessed under 200 keV electron irradiation [5]. Conversely, Rai and co-workers have observed a substantial enhancement in the wear life of the WS_2 coating on steel, even up to several folds when irradiated with 2.5 MeV Ag ions [6]. In contrast, the work of Chen *et. al.* on 60 keV Ar^+ ion irradiation on the atomically thin WS_2 sheets has resulted in tailored optical properties of the WS_2 monolayer via creation and manipulation of S- vacancies [7]. Recently, 600 keV and 6 MeV O ion irradiation effect on the WS_2 nanosheets was shown to alter the number of layers, thickness and optical band gap of the WS_2 nano sheets [8]. Thus, post irradiation effect of these layered systems, have seemingly large opportunity to exploit modified structural, optical and mechanical properties at large.

In this chapter, we highlight formation and splitting of stacks of WS_2 nanosheets into a few layer systems under 80 keV Xe^+ ion irradiation at normal incidence. The micro-morphological, visible emission response, Raman active

vibronic modes and wettability features are analysed and discussed, on a comparative basis.

6.1 Irradiation experiment on WS_2 nanosheets

Multilayer WS_2 nanosheets have been synthesized using a facile, hydrothermal method followed by ultrasonication. In order to perform irradiation experiment, the as- prepared WS_2 product was allowed to impregnate on a teflon pellet. For this purpose, a thin teflon tape was crushed into the shape of a circular disc of diameter ~1 cm and then, the WS_2 powder is sprinkled over it. The sprinkled powder was made to stick to the teflon pellet by hot pressing using a hydraulic press. The prepared specimens as shown in Fig. 6.1 , were subjected to 80 keV Xe^+ ion irradiation using the low energy ion beam facility (LEIBF) available at IUAC, New Delhi. A constant beam current of ~2 μA was maintained throughout the experiment while the fluence was varied as, 1×10^{15} (F_1), 5×10^{15} (F_2), 1×10^{16} (F_3) and 5×10^{16} (F_4) ions/cm^2. The projectile ranges, electronic energy loss (S_e) and nuclear energy loss (S_n) of the WS_2, teflon and WS_2/teflon systems were calculated using the SRIM 2008® software [11]. The physical properties of the specimens are highlighted in Table 6.1.

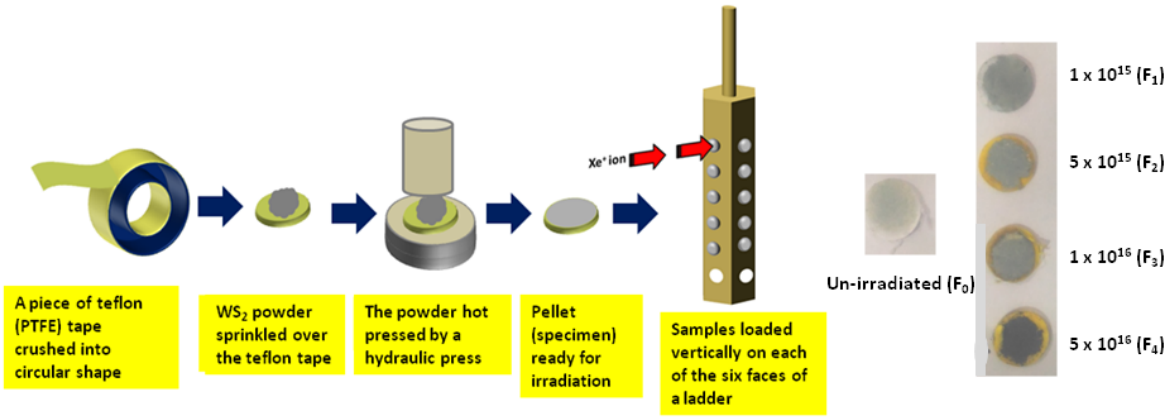

Figure 6.1: The schematic representation of the preparation of samples for the irradiation experiment along with the digital photographs of the un-irradiated and post irradiated samples, shown at the extreme right.

Table 6.1: Electronic and nuclear energy losses and projectile ranges of ions in target materials

Material	Density (g/cc)	S_e (eV/Å)	S_n (eV/Å)	S_n/S_e	Projectile range (Å)	Straggling (Å)
Teflon	2.2	24.13	211.9	~8.8	433	123 (longitudinal), 104 (lateral)
WS_2	7.5	28.43	310.10	~10.9	223	112 (longitudinal), 82 (lateral)

6.2 Post-irradiation analyses

Powder X-ray diffraction (XRD) technique was employed to reveal information regarding crystallography aspects for which a MiniFlex Rigaku X-ray diffractometer equipped with a CuK_α source (K_α = 1.543 Å) was employed. The morphological details of the pristine and irradiated systems were revealed both through scanning electron microscopy (SEM, JEOL JSM, 6390 LV) and transmission electron microscopy (HRTEM, JEOL, JEM-2100) imaging studies. Energy dispersive X-ray analysis was carried out to understand the elemental composition of the synthesised product. Whereas, surface morphologies were further assessed by atomic force microscopy (AFM, NTEGRA Vita- NT-MDT), the phonon-assisted vibrational modes are exploited with the help of a Raman spectrometer (Chemlogix, EZRaman-N) by employing ~785 nm excitation line of the Ar^+ laser. On the other hand, photoluminescence spectra and optical absorption characteristics were acquired on a luminescence spectrophotometer (Hitachi 2700 FL) and a UV–Vis spectrophotometer (UV 2450, Shimadzu Corporation); respectively.

6.2.1 Microstructure and surface morphology

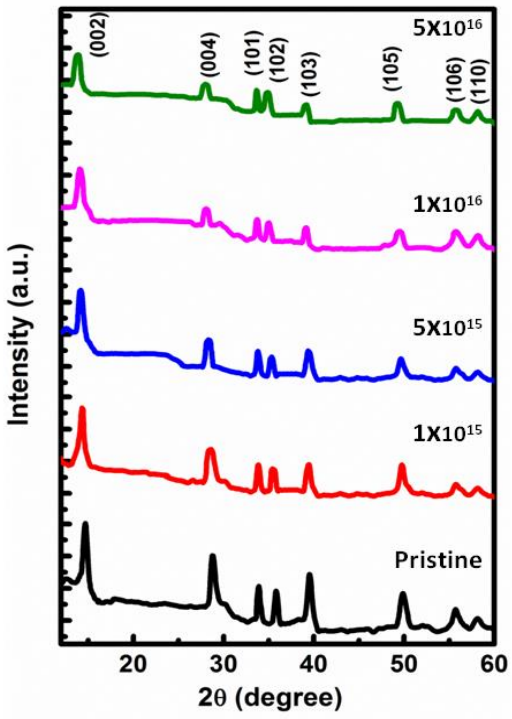

Figure 6.2: XRD patterns of the un-irradiated and irradiated nano-WS_2 samples.

Powder XRD patterns of the un-irradiated (pristine) and the irradiated nano-WS_2 systems are shown in Fig. 6.2. The prominent peaks, observed at $2\theta \sim 14.65^0$ and 28.82^0 are attributed to (002) and (004) planes of the hexagonal phase of WS_2 (JCPDS File No.08-0237) [11]. Upon irradiation, the peak intensity of these peaks decreases with increase in ion fluence. Also the peaks have been found to shift towards the lower Bragg's angle with the magnitude of ion fluence. An apparent increase in the full width half maxima (FWHM) has also been witnessed. The decrease in the peak intensity with the increased FWHM value is attributed to the declining crystallinity as a result of which fragmentation occurred due to energetic ion impact [12]. The change in the lattice parameter of the irradiated samples can be related to the strain produced in the samples as a result of irradiation [12]. We have also calculated the micro-strain (ε) in the un-irradiated and irradiated samples using the relation $\varepsilon = \beta \cos\theta/4$. It was found that the micro-strain values tend to increase with increase in the ion fluence, as a result of which the lattice parameters would vary substantially.

The structural parameters associated with the un-irradiated and irradiated samples are enlisted in the table as given below.

Table 6.2: Structural parameters obtained through XRD analyses

Ion fluence (ions/cm^2)	Intensity of the main (002) peak (a.u.)	FWHM (degree)	Lattice constant (Å)	Micro-strain ($\times 10^{-3}$)	Average Crystallite size (nm)
Pristine	740.9	0.429	a=3.13, c= 12.12	1.86	19.5±0.9
F1: 1× 10^{15}	596.4	0.521	a=3.15, c= 12.37	2.25	16.1±1.3
F2: 5× 10^{15}	541.9	0.592	a=3.17, c= 12.47	2.56	14.2±0.8
F3: 1× 10^{16}	514.7	0.685	a=3.18, c= 12.57	2.96	12.2±1.0
F4: 5× 10^{16}	490.1	0.774	a=3.19, c= 12.80	3.35	10.8±1.1

As can be seen from Fig. 6.3 (a), the TEM micrographs of the pristine WS_2 consists of stacks of nano-sheets, with occasional instances of tubular and plate like morphologies. The large mass of sheets got fragmented, both in dimension and thickness when exposed to 80 keV Xe^+ ion irradiation (Fig. 6.3 (b-e)). Whereas, the first and second columns depict representative micrographs at lower and higher magnifications, respectively. At the highest fluence (F4), the average size of the stack of nano-sheets becomes as small as ~20 nm, implying thereby only a few layer systems. As compared to pristine WS_2, the irradiated ones exhibited unclear lattice fringes which could be due to the sputtering of the sulphur atoms by the impact of Xe^+ ions [13]. Moreover, distinct bright spots around the central zone in the SAED spectrum of the pristine turn into diffused ring patterns after ion irradiation. This clearly demonstrates the lack of adequate atomic planes and introduction of disorder needed to cause diffraction effect and consequently, the loss of crystallinity in the irradiated nano-WS_2 systems [13, 14]. Likewise, oxygen vacancies are inherent to oxide systems; sulphur vacancies are common in chalcogenides owing to the low vapour pressure of the sulphur

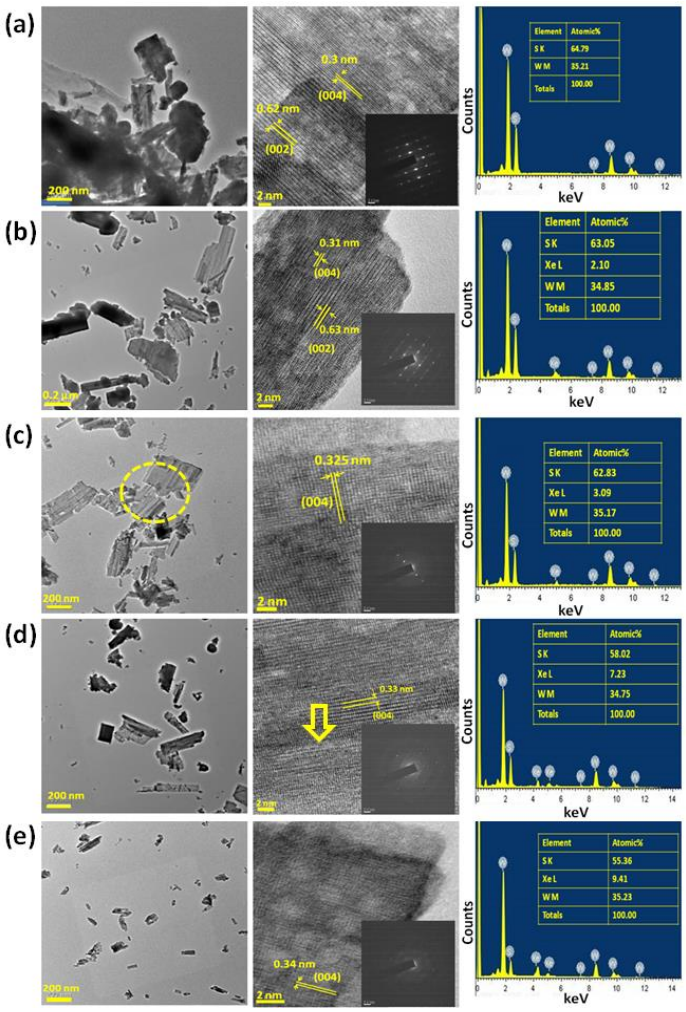

Figure 6.3: TEM micrographs of (a) un-irradiated and irradiated nano-WS_2 samples with a fluence variation of (b) 1×10^{15}, (c) 5×10^{15}, (d) 1×10^{16}, (e) 5×10^{16} ions/cm^2, while SAED patterns are shown as insets in the mid-column figures. The splitting of nano-stacks into sheets and lattice fringes are evident at higher magnifications. The EDX spectra of the respective systems, with elemental energy spikes are depicted in the extreme right column.

atoms relative to its metal counterpart. A clear signature of the sputtering out of the S atoms from the irradiation-led thermodynamically unstable WS_2 lattice is quite apparent from the EDX spectra which showed a drastic fall in the sulphur content (right column, Fig. 6.3 (a-e)). The typical S-to-W ratio drops from a value of 1.84 to 1.57 with an increase in irradiation fluence [4]. At a specific site, the average lowering of S atoms, was to the tune of ~14% which eventually implies the introduction of adequate sulphur vacancies due to the splitting of the stack of WS_2 into a few layer systems.

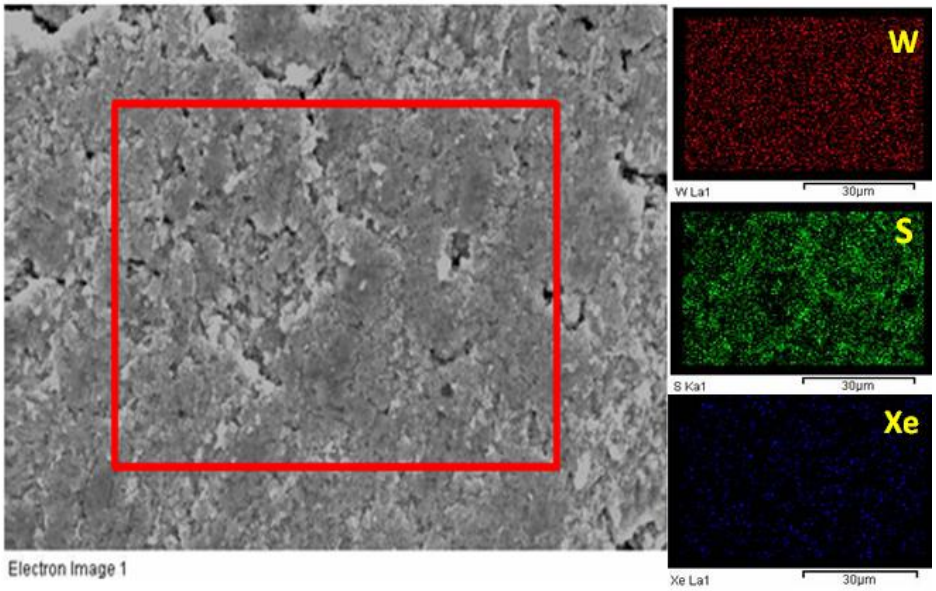

Figure 6.4: Elemental mapping of the sample F4, which illustrates the distribution of W, S and Xe sites spread over an approximate area of 70 µm x50 µm.

The elemental mapping of the post-irradiated nano-WS_2 system (F4) was examined for an area 70 µm x 50 µm, and depicted in Fig. 6.4. The images clearly indicate the presence of W, S and Xe^+ in the specimen. Representing the first two elements, while the red and green spots are quite prominent over a uniform spread area, the implantation of Xe^+ species was evident from the faint, blue-marked mapping.

The schematic representation of the impact of ion irradiation on the WS_2 nanosheets is shown in Fig. 6.5. The two and three- dimensional (2D and 3D) surface morphologies of the pristine and Xe^+ ion irradiated WS_2 nano-sheets were exploited by employing the AFM technique, operating in semi-noncontact mode and analyzed with the help of *Gwyddion software*® [17]. The AFM images, depicted in Fig. 6.6 A (a-e), have revealed the occurrence of a few to multi layers present in stacks, while displaying smooth topology of the pristine WS_2.

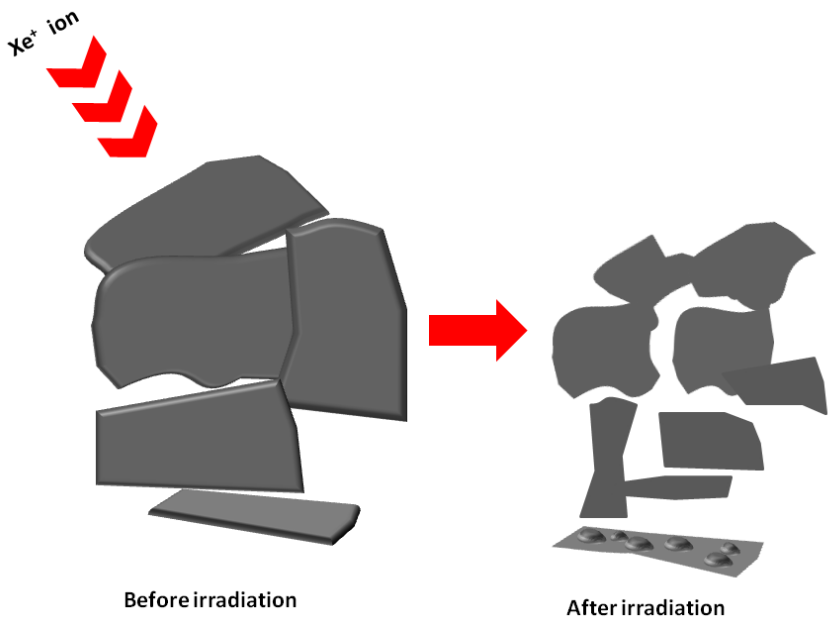

Figure 6.5: Schematic representation of the impact of irradiation on the WS_2 sheets.

However, it offered quite a few hillocks and craters after prolonged impact of ions. The breaking of stack of WS_2 into pieces and digging out of surface atoms as a result of ion bombardment have been anticipated in this situation and consequently, surface roughness is quite prominent in the post-irradiated specimens. The transition from a superbly smooth surface of the stack of WS_2 into a relatively rough one for the fragmented sheets could be visualized easily in the 3D micrographs, shown in the central column of Fig. 6.6 A (a). The root mean squared roughness (R_q) was found to vary in the range 103.1- 211.8 nm with increasing ion fluence. The nature of inclusion of Xe, loss of sulphur atoms, and R_q are plotted collectively, as a function of ion fluence, and highlighted in Fig. 6.6 A (b). Apparently, the roughness developed at higher fluences, was expected to be due to the creation of sulphur point defects owing to the loss of adequate S atoms and local deformation while massive splitting due to impact of energetic Xe^+ was in progress.

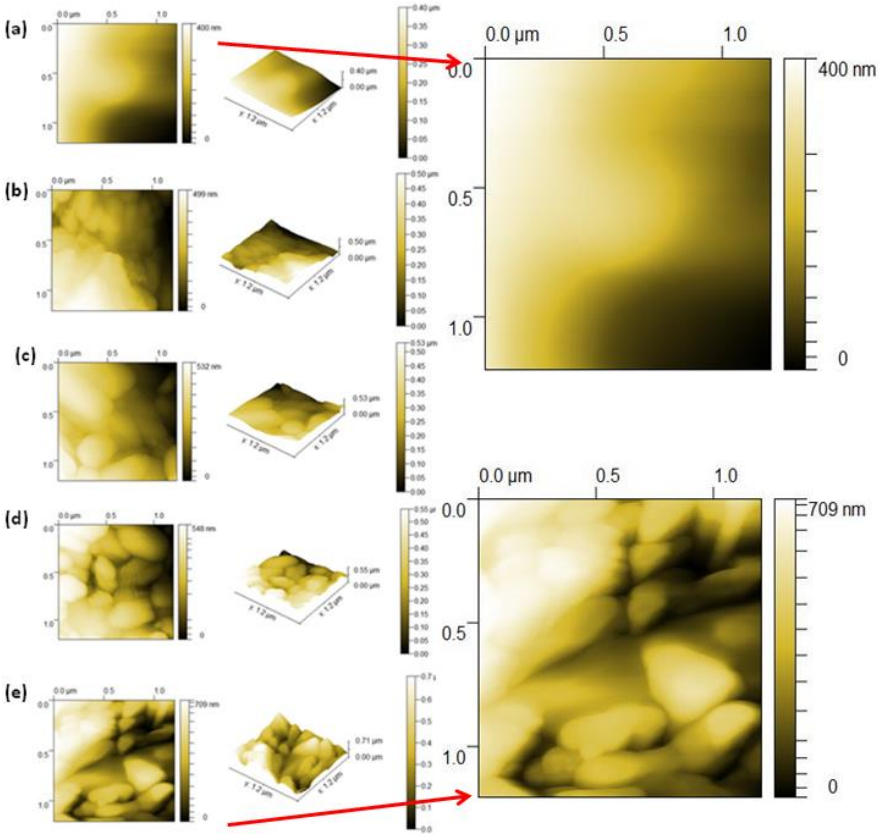

Figure 6.6 A: 2D and 3D AFM images of the (a) un-irradiated (F0) and irradiated nano-WS_2 systems subjected to a fluence variation of (b) 1×10^{15} (F1), (c) 5×10^{15} (F2), (d) 1×10^{16} (F3), (e) 5×10^{16} (F4) ions/cm^2. The magnified 2D images of pristine (F0) and irradiated (F4) nano-WS_2 are also shown on the right hand side.

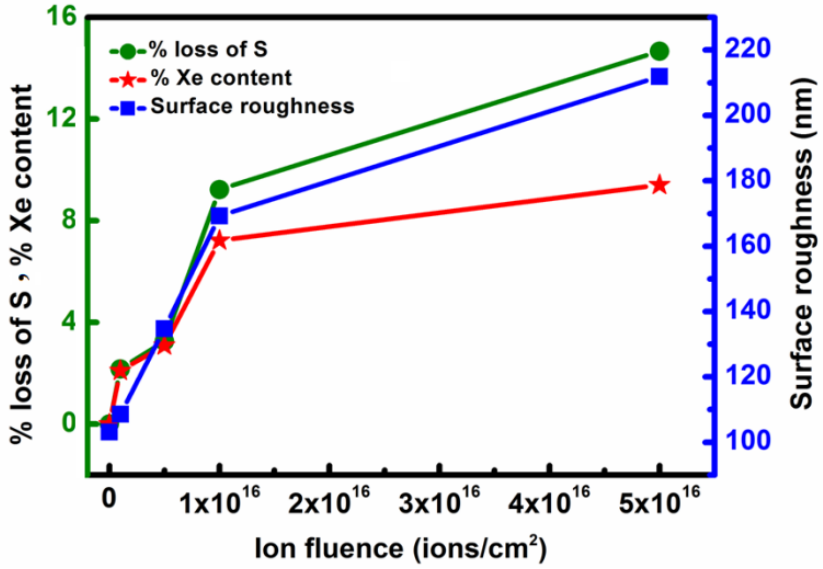

Figure 6.6 B: The variation in % S loss, % Xe content and surface roughness with increasing ion fluence.

6.2.2 Radiative emission, Stoke's shift and Raman modes

Both the un-irradiated and post-irradiated nano-WS_2 samples exhibited noticeably broad, visible photoluminescence (λ_{ex}=450 nm) spectra, with the emission peak positioned at, λ_{em} ~633 nm (Fig. 6.7 (a)). Although the PL intensity was reported to increase with size reduction [15], here we are unsure about this tricky goal of comparing intensity of emission in terms of obtained nanoscale geometry and dimension. This is because, the strength of emission is directly linked to the number of radiative recombination events occurring in the system and that, it was quite difficult to control these in terms of number density of the fragmented sheets. However, full width at half maxima (FWHM) and symmetry factor (σ) could be easily estimated, as shown in Table 6.3. Shown schematically in Fig. 6.7 A (b), the left (σ_L) and right symmetry (σ_R) factors are defined as [16],

$$\sigma_L = \frac{\lambda_m - \lambda_L}{\lambda_R - \lambda_L} \quad \text{and} \quad \sigma_R = \frac{\lambda_R - \lambda_m}{\lambda_R - \lambda_L} \qquad (6.1)$$

such that, $\sigma_L + \sigma_R = 1$.

Here, $\sigma_L \neq \sigma_R$ demands absolute symmetry in the spectral response. Also, λ_R and λ_L is the FWHM and symbols representing their usual meanings (λ_m is the wavelength of peak maximum) (Fig. 6.7 (b)). Here, with an increase in ion fluence, we noticed a fall in left symmetry and consequent enhancement in right symmetry factor (Table 6.3).

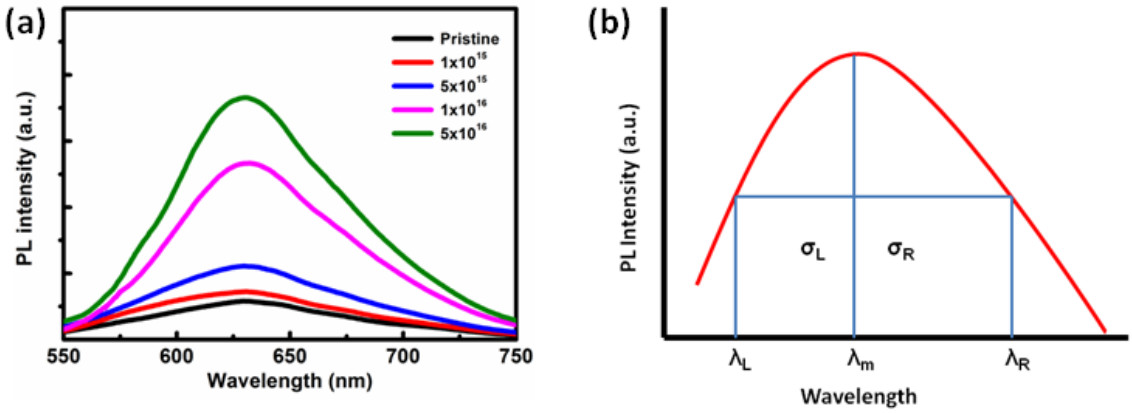

Figure 6.7: PL spectra of (a) un-irradiated (F0), and irradiated nano-WS_2 systems subjected to a fluence variation of 1× 10^{15} (F1), 5× 10^{15} (F2), 1× 10^{16} (F3), 5× 10^{16} (F4) ions/cm^2. The schematic of an asymmetric PL response with symmetry factors is shown in (b).

Table 6.3: Physical parameters obtained from the optical absorption and PL spectra

Sample	Peak position (nm)	FWHM (nm)	Symmetry factor		Stoke's shift, Δ (eV)	$S_p = \frac{\Delta}{2\hbar\omega_{LO}}$
			σ_L	σ_R		
F0	633.1	108.3	0.455	0.545	0.013	0.15
F1	632.2	103.1	0.452	0.548	0.030	0.35
F2	631.3	101.9	0.444	0.556	0.037	0.43
F3	630.8	92.6	0.388	0.612	0.087	1.01
F4	628.5	89.1	0.381	0.619	0.141	1.64

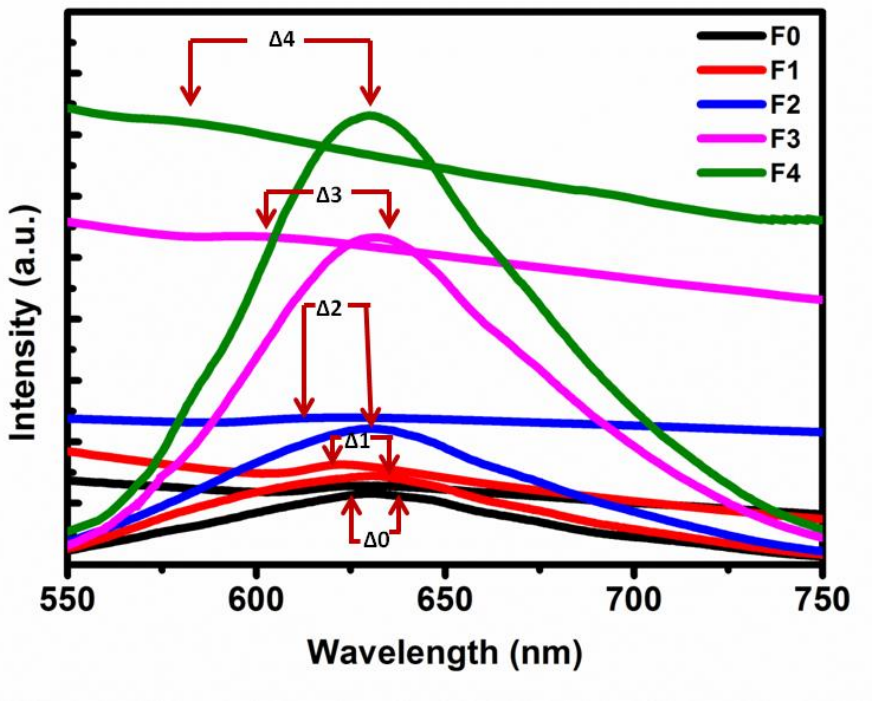

Figure 6.7 (c): Stokes shift shown for the un-irradiated and irradiated nano-WS_2 samples (F0-F4).

Thus, the introduction of new origin of radiative recombination events could be anticipated, apart from direct recombination of carriers. We assign these to surface defects and trap states, which form as a consequence of ion irradiation

effects. The Stokes shift, which is a measure of the strength of electron-phonon coupling, can be determined by analysing optical absorption and luminescence spectra (Fig. 6.7 (c)). The difference in absorption and emission energy maxima, as revealed through the Frank-Condon principle [17],

$$\Delta = \frac{hc}{\lambda_{ab}} - \frac{hc}{\lambda_{em}} = 2S_p\,\hbar\omega_{LO}, \qquad (6.2)$$

where, λ_{ab} and λ_{em} characterize the associated wavelengths of absorption and emission maxima; respectively. Also, $\hbar$ is the reduced Planck's constant, ω_{LO} is the longitudinal optical (LO) phonon frequency (for WS_2, ω_{LO} =345.9 cm^{-1} [18]) and S is the electron-phonon coupling constant. A drastic increase in S_p value from 0.15 to as high as, 1.64 accounts for an invariable increase in the Stoke's shift and consequently, strong electron-phonon interaction in the irradiated nano-WS_2 (Table 6.3) [19].

The Raman active, vibrational modes of the un-irradiated and irradiated nano-WS_2 systems, can be found in Fig. 6.8. Apparently, the pristine nano-WS_2 gave $E_{2g}^1$and A_{1g} modes located at ~351.2 cm^{-1} and 415.6 cm^{-1}; respectively. While the former is typical to describe in-plane vibrations of the W and S atoms bonded covalently, the A_{1g} mode would emerge as a consequence of out-of-plane vibrations of the S atoms linked via van der Waal's bonding [15]. As can be found from Fig. 6.7 and Table 6.4, with irradiation, these peaks tend to shift slightly towards a higher wavenumber, in proportion to the increasing ion fluence. Notably, the E_{2g}^1-to-A_{1g} Raman intensity ratio has increased from 0.72 to 0.87, with a progressive increase in ion fluence. Earlier, the blue-shifting of the Raman active peaks was attributed to the exfoliation of nano-WS_2 as a result of energetic ion impact [20]. It was anticipated that, the exfoliation occurred as a result of weakening of the van der Waal's interaction among the subsequent layers and consequently, a decline in the restoring force is capable of exhibiting the desired blue-shift of the peaks [20]. An apparent increase in the E_{2g}^1-to-A_{1g} Raman intensity ratio along with manifested FWHM values with the impact of irradiation, in fact, suggest breaking of stack of nano-WS_2 and eventually, formation of few layer nanosheets.

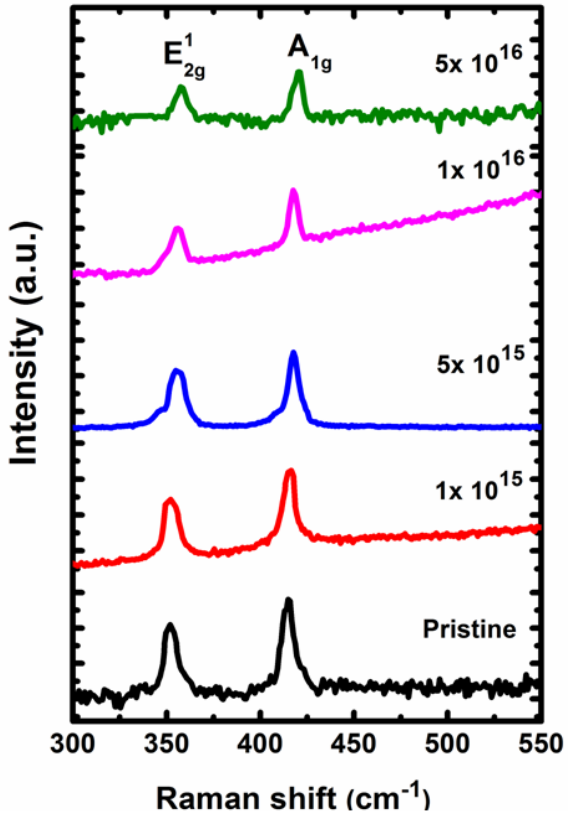

Figure 6.8: Raman spectra of (a) un-irradiated (F0), and irradiated nano-WS_2 systems: (b) 1×10^{15} (F1), (c) 5×10^{15} (F2), (d) 1×10^{16} (F3), (e) 5×10^{16} (F4) ions/cm^2.

Table 6.4: Raman active modes and mode-assignment

Sample	Peak position (cm^{-1})		FWHM (cm^{-1})		E^1_{2g}/A_{1g}
	E^1_{2g}	A_{1g}	E^1_{2g}	A_{1g}	
F0	351.3	415.3	8.4	7.3	0.72
F1	352.5	415.9	8.7	7.5	0.77
F2	354.7	417.2	9.6	7.7	0.82
F3	356.1	417.4	10.1	7.9	0.84
F4	357.3	419.3	10.3	8.1	0.87

6.2.3 Transition from hydrophilic (wetting) to hydrophobic (dewetting) surface features

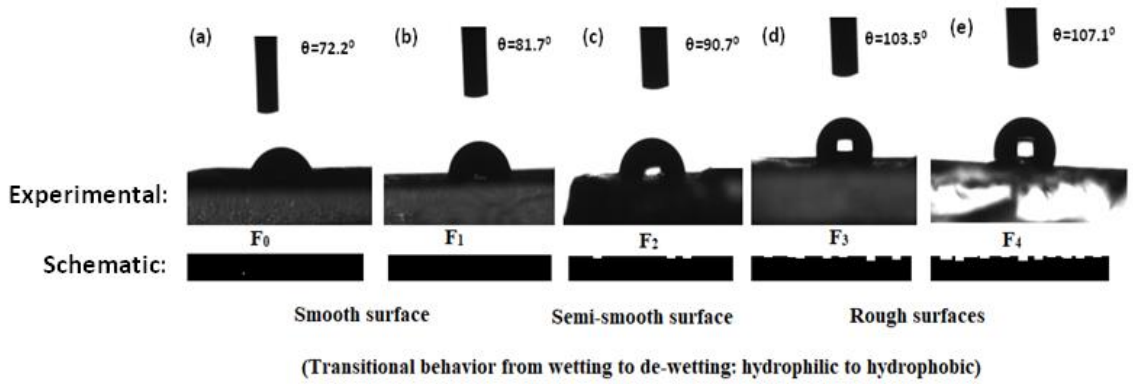

Figure 6.9: Static water contact angle (CA) values measured at the surfaces of un-irradiated and irradiated nano-WS_2 systems. Note the progressive increase in CA with increasing ion fluence from F1 to F4: F1= 1×10^{15} , F2= 5×10^{15} ,F3= 1×10^{16} , F4= 5×10^{16}

The wettability property of a surface is essentially determined by assessing the droplet shape and consequently, water contact angle (CA). The droplet shape and static water CA of the pristine and irradiated nano-WS_2 systems are shown in the upper panel of Fig. 6.9. Offering a CA of 72.2°, the un-irradiated nano-WS_2 was found to be just hydrophilic ($\theta<90°$). The F1 specimen exhibiting a higher CA (81.7^0) as compared to the pristine one. In contrast,CA increases to 90.7° for the specimen irradiated at a fluence of $5x10^{15}$ ions/cm^2 (F2), and thus the surface is at the boundary of wetting-de-wetting transition. Nevertheless, the water CA is substantially increased, to 103.5° and 107.1° in case of specimens irradiated at higher fluences (F3 and F4). Thus, attributed to surface roughness, a clear transition from the hydrophilic to hydrophobic nature is quite evident with increasing ion fluence, which are schematically shown at the lower panel of Fig. 6.9.

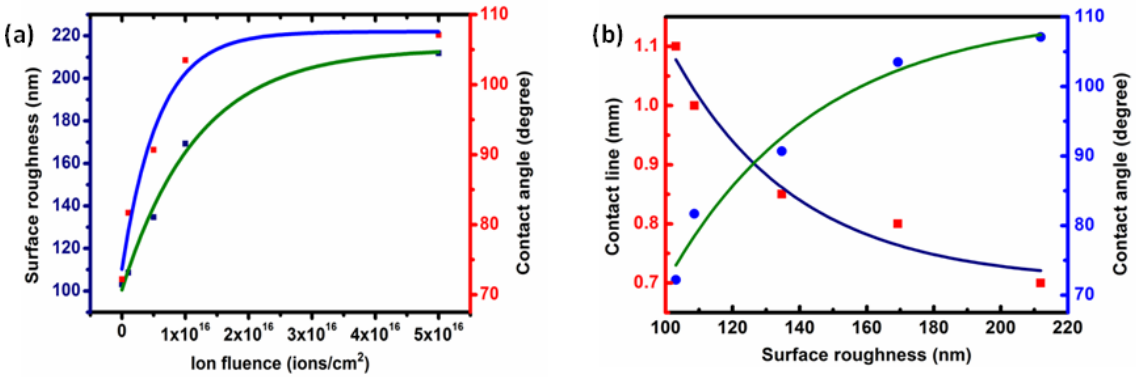

Figure 6.10: (a) Variation of the CA and roughness with increasing ion fluence, (b) variation of contact line and CA with surface roughness.

The respective microscopic and macroscopic data acquired by virtue of AFM and contact angle measurements, are plotted together, in Fig. 6.10. Here, the variation in contact-line (l_t), CA and R_q with increasing ion fluence has been shown. Here the contact line is defined as the diameter of the circular contact line below the water droplet kept on a given surface [21]. Since, it is the roughness which is believed to affect wettability, contact-line and CA were also plotted as a function of R_q (Fig. 6.10 (b)). While the variation of l_t exhibited an exponentially decaying trend, the CA predicts an associated exponentially growing trend, which yielded empirical relations:

$$\left.\begin{aligned} &y_1 \sim \eta\, exp(-\alpha x), \text{ with fitting value, } \alpha = 27\ \mu m^{-1} \\ &y_2 \sim \eta\, (1-exp(-\beta x)), \text{ with fitting value, } \beta = 35\ \mu m^{-1} \end{aligned}\right\} \quad (6.3)$$

and η is a system dependent parameter. It is quite apparent that, contact line tends to shrink with the surface roughness as air-pockets beneath the droplet would prevent it from wetting. Thus the stack of nano-sheets, which fragment into several layer nano-sheets, are more rough at the microscopic level due to the dislodgement of atoms from the surfaces, which could result in adequate hydrophobicity/dewetting feature.

6.3 Conclusion

To conclude, 80 keV Xe^+ ion irradiation has led to splitting of nano-WS_2 stacks into smaller, still several layered nano-sheets, a subsequent increase in rms roughness, manifested PL and Raman spectra and wetting de-wetting transitional responses. Exhibiting a hexagonal crystal structure, the large stack of nano-sheets were found to get splitted both in terms of thickness and coverage area, as revealed from TEM imaging studies. The elemental analysis, as obtained through the EDX spectra has indicated sulphur deficient surfaces in the post-irradiated specimens, suggesting a drop in the S-to-W ratio, from 1.85 to 1.57. Moreover, the AFM images are capable of displaying surface topology with numerous hillocks and ripple like structures after incorporation of Xe^+, while destroying the smoothness of the film surface. The Raman study affirms the exfoliation of the nano-systems as a result of irradiation. The Stokes shift is significantly enhanced as evidenced from the increase in electron-phonon coupling parameter, $S_p > 1$. A clear hydrophilic to hydrophobic transition, as a result of improved surface roughness, caused by normal ion irradiation has also been witnessed.

References

[1] Krasheninnikov, A. V., Nordlund, K. Ion and electron irradiation-induced effects in nanostructured materials. *Journal of Applied Physics*, 107:071301, 2010.

[2] Avasthi, D.K., Mehta, G.K. Swift Heavy Ions for Materials Engineering and Nanostructuring, Springer Series in materials science, Springer Netherlands, 2011

[3] Li, Z., Chen, F. Ion beam modification of two-dimensional materials: Characterization, properties, and applications. *Applied Physics Reviews*, 4:011103 ,2017.

[4] Wang, Y., Feng, Y.,Chen, Y., Mo, F., Qian, G., Yu, D., Wang, Y., Zhang, X. Morphological and structural evolution of WS_2 nanosheets irradiated with an electron beam. *Physical Chemistry Chemical Physics*, 17:2678-2685, 2015.

[5] Ding, K., Feng, Y., Huang, S., Li, B., Wang, Y., Liu H., Qian, G. The effect of electron beam irradiation on WS_2 nanotubes. *Nanotechnology*, 23:415703, 2012.

[6] Rai, A., Bhattacharya, R., Zabinski, J., Miyoshi, K. A comparison of the wear life of as-deposited and ion-irradiated WS_2 coatings. *Surface and Coatings Technology,* 92:120, 1997.

[7] Ma, L.N., Tan, Y., Ghorbani-Asl, M., Boettger, R., Kretschmer, S., Zhou, S.Q., Huang, Z.Y., Krasheninnikovb, A.V., Chen, F. Tailoring Optical Properties of Atomically-Thin WS_2 via Ion Irradiation. *Nanoscale*, 9:11027-11034**,** 2017.

[8] Song, H., Yu, X., Chen, M., Qiao, M., Wang, T., Zhang, J., Liu, Y., Liu, P., Wang, X. Modification of WS_2 nanosheets with controllable layers via oxygen ion Irradiation. *Applied Surface Science*, 439:240–245, 2018.

[9] Zeigler, J. The Stopping Range of Ions in Matter, SRIM-2008 (2008).

[10] Pan, L., Liu, Y-T., Xie, X-M., Ye, X-Y. Facile and Green Production of Impurity-Free Aqueous Solutions of WS_2 Nanosheets by Direct Exfoliation in Water. *Small*, *12:*6703–6713, 2016.

[11] Som, S., Sharma, S.K., Lochab, S.P. Swift heavy ion induced structural and optical properties of Y_2O_3:Eu^{3+} nanophosphor. *Materials Research Bulletin*, 48:844, 2013.

[12] Gotoh, Y., Shimizu, H., Murakami, H. High resolution electron microscopy of graphite defect strucwres after keV hydrogen ion bombardment. *Journal of Nuclear Materials*, 162-164: 851-855, 1989.

[13] Som , S., Dutta, S., Kumar, V., Kumar, V., Swart, H.C., Sharma, S.K. Swift heavy ion irradiation induced modification in structural, optical and luminescence properties of Y2O3:Tb^{3+} nanophosphor. *Journal of Luminescence*, 146:162–173, 2014.

[14] URL http://gwyddion.net/

[15] Nguyen, T. P., Sohn, W., Oh, J.H., Jang, H.W., Kim, S.Y. Size-Dependent Properties of Two-Dimensional MoS_2 and WS_2. *Journal of Physical Chemistry C*, 120:10078−10085, 2016.

[16] Bayan, S., Das, U., Mohanta, D. Development of Tb-doped ZnO nanorods: Effect of nitrogen ion irradiation on luminescence and structural evolution. *Physica Status Solidi A,* 207, 1859-1863, 2010.

[17] Mohanta, D., Ahmed, G.A., Dolui, S.K., Avasthi, D.K., Choudhury, A. Effect of 160 MeV Ni^{12+} ion irradiation on PbS quantum dots. *Journal of Luminescence*, 114:95-100, 2005.

[18] Sohier, T., Calandra, M., Mauri, F. Two-dimensional Fröhlich interaction in transition-metal dichalcogenide monolayers: Theoretical modeling and first-principles calculations. *Physical Review B*, 94:085415, 2016.

[19] Mooser, E. (auth.), Butcher, P. N., March, N. H., Tosi, M. P. (eds.) *Crystalline Semiconducting Materials and Devices*, 1st edition, Springer US, 1986.

[20] Molina-Sanchez, A., Wirtz, L. Phonons in single-layer and few-layer MoS_2 and WS_2. *Physical Review B,* 84:155413-1-8, 2011.

[21] Cassie, A.B.D. Contact angles. *Discusssions of the Faraday Society,* 3:11-16, 1948.